ACS APPLIED MATERIALS & INTERFACES

Research Article

www.acsami.org

Self-Assembly of Diblock Copolymer–Maghemite Nanoparticle Hybrid Thin Films

Yuan Yao,[†] Ezzeldin Metwalli,[†] Jean-François Moulin,[‡] Bo Su,[†] Matthias Opel,[§] and Peter Müller-Buschbaum*[,†]

[†]Technische Universität München, Physik-Department, Lehrstuhl für Funktionelle Materialien, James-Franck-Str. 1, 85748 Garching, Germany

[‡]Helmholtz Zentrum Geesthacht, Institut für Werkstoffforschung, Abteilung WPN, Instrument REFSANS, MLZ, Lichtenbergstrasse 1, 85748 Garching, Germany

[§]Walther-Meissner-Institut, Bayerische Akademie der Wissenschaften, Walther-Meissner-Straße 8, 85748 Garching, Germany

Supporting Information

ABSTRACT: The arrangement of maghemite (γ-Fe_2O_3) nanoparticles (NPs) in poly(styrene-d8-*block*-*n*-butyl methacrylate) P(Sd-*b*-BMA) diblock copolymer (DBC) films via a self-assembly process was investigated toward the fabrication of highly ordered maghemite–polymer hybrid thin films. The resulting thin films exhibited a perforated lamella with an enrichment layer containing NPs as investigated with X-ray reflectometry, scanning electron microscopy, atomic force microscopy, and time-of-flight grazing incidence small angle neutron scattering as a function of the NP concentrations. The NPs were selectively deposited in the PSd domains of the DBC during the microphase separation process. At low NP concentrations, the incorporation of the NPs within the DBC thin films resulted in an enhanced microphase separation process and formation of highly oriented and ordered nanostructured hybrid films. At higher NP concentrations, the aggregation of the NPs was dominating and large sized metal oxide clusters were observed. The superparamagnetic properties of the metal oxide–polymer hybrid films at various NP concentrations were probed by a superconducting quantum interference device magnetometer, which shows that the hybrid films are highly attractive for optical devices, magnetic sensors, and magnetic recording devices.

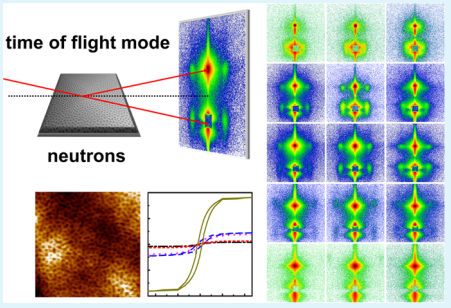

KEYWORDS: *maghemite nanoparticle, TOF-GISANS, block copolymer, thin film, self-assembly*

1. INTRODUCTION

Doping various types of functional nanoparticle (NP) fillers into a polymer matrix produces hybrid materials with interesting thermal, mechanical, electric, optical, or magnetic properties, which offer great versatile applications such as thermoplastic resins, solar cells, sensors, packaging, target drug delivery, metal catalysis, and magnetic storage devices.[1−9] Generally, the main advantage of NPs arises from the high surface-to-volume ratio.[10] Particularly, applications using maghemite NPs (γ-Fe_2O_3) profit from the low magnetic remanence and coercivity compared with those of bulk magnetic material, such as in medical applications and high-density memory devices.[1,11,12] Diblock copolymers (DBCs) are powerful and promising tools for the manufacture of diverse nanoscale ordered structures via a low-cost, highly efficient self-assembly method.[13,14] The tuning of the polymer domain spacing in the range of 10−100 nm can be achieved by selecting the molecular weight and the chemistry of the polymer blocks.[15] An ordered, highly periodic polymer template is essential for producing well-defined metal oxide–polymer nanocomposites.[16−18] Employing the selective metal oxide NP deposition in one block of the DBC films enables a highly ordered metal oxide NP distribution within the polymer film. Both enthalpic and entropic interactions, such as metal oxide–metal oxide interactions play important roles on the overall spatial distribution of the metal oxide NPs within the polymer matrix.[19,20] Morphological modifications of the nanostructured DBC films upon incorporation of the metal NPs has been reported.[21] For instance, Lo and Lin investigated the alignment of magnetic pyridine-grafted Fe_2P nanorods in P(S-*b*-VP) DBC as functions of both the nanorod concentration and the length of the long-axis of the nanorods.[22] The nanorods selectively deposit into the PVP domains and follow the polymer morphology at short lengths, whereas large aggregates at long lengths and high concentrations of the metal nanorods were observed.[22] Aissou et al. showed that the dopamine-terminated methoxy poly(ethylene oxide) coated FePt NPs are deposited into the spherical PEO domains of the P(S-*b*-EO) DBC by employing a toluene/water solvent annealing process.[23] Akcora et al. investigated the morphology of norbornene (NOR)/deuterated norbornene dicarboxylic acid (NORCOOH) DBC with varied block volume fractions upon the incorporation of

Received: August 1, 2014
Accepted: September 22, 2014
Published: September 22, 2014

Fe_2O_3 NPs.[24] The interactions between metal oxide NPs and polymer lead to deformation of the initial spherical morphology of the DBC.[24]

In previous investigations, we have already studied several hybrid nanocomposite systems based on different types of PS-coated inorganic iron oxide NPs and DBCs.[25−28] In the present work, we aim at investigating the nanomorphology of poly(styrene-d8-*block*-*n*-butyl methacrylate) P(Sd-*b*-BMA) DBC films in relation to the incorporated maghemite NPs for the special morphology of a perforated lamella with an enrichment layer containing NPs. Using real-space techniques, such as atomic force microscopy (AFM) and scanning electron microscopy (SEM), and reciprocal-space techniques, such as X-ray reflectivity (XRR) and time-of-flight grazing incidence small angle neutron scattering (TOF-GISANS), the film structure is probed. The time-of-flight (TOF) mode enables simultaneous, nondestructive GISANS measurements at many different wavelengths in a single experiment.[29,30] By utilizing a variation of wavelengths of the neutron beam, the complex inner structures are determined at different depths in the probed samples.[29,31,32] With this unique technique, various film depths are simultaneously accessible, and additional structural information such as possible polymer enrichment at either polymer−air or polymer−substrate interfaces and the DBC/NPs morphological correlation can be probed.[33,29] The magnetic properties of the hybrid films were probed with a Quantum Design magnetic property measurement system. In the present study, a unique "hybrid structure", which consists of a single iron-oxide-doped PSd layer at the polymer−substrate, perforating a top PBMA layer, is achieved.

2. EXPERIMENTAL SECTION

2.1. Sample Preparation. The DBC poly(styrene-d8-*block*-n-butyl methacrylate), denoted P(Sd-*b*-BMA), was purchased from Polymer Standard Service GmbH (Mainz, Germany) and used without any further purification. The number-average molecular weight of P(Sd-*b*-BMA) and weight fraction of PSd were 158 kg/mol and 0.53, respectively. The polydispersity was $M_w/M_n = 1.18$. On the basis of the theoretical phase diagram of DBCs, a lamella morphology is expected for the bare P(Sd-*b*-BMA) bulk sample.[34] We have used deuterated PS so that the scattering length densities of the involved materials, PSd = 5.99×10^{-4} nm^{-2}, PBMA = 5.54×10^{-5} nm^{-2}, and Fe_2O_3 = 7.18×10^{-4} nm^{-2} have significant neutron contrast for the TOF-GISANS experiment. The Flory−Huggins segment−segment interaction parameter (χ) of PS and PBMA is 0.015 at room temperature.[35] Thus, the probed DBC is in the intermediate segregation regime ($\chi N \approx 44$). PS-coated maghemite NPs (γ-Fe_2O_3) were synthesized using α-lithium polystyrenesulfonate (LPSS, obtained from Heidelberg University, Heidelberg, Germany). The NPs synthesis protocols were described in detail elsewhere.[36] The mean diameter of the NPs was 6.6 nm with a log-normal size distribution (width = 0.2). The size and the chemical identity of the employed NPs were examined using small-angle X-ray scattering (SAXS) and Mössbauer techniques. These results are provided in Figures S1 and S2 (Supporting Information).

Silicon substrates (Si 100, *n*-type, Silchem) were cut into pieces (7 × 7 cm^2) and immersed into an acid cleaning bath (200 mL of H_2SO_4, purity 95%; 70 mL of H_2O_2, purity 30%; and 130 mL of deionized water) at 80 °C for 15 min, followed by vigorous rinsing with deionized water and subsequent drying with N_2 gas.[37] Different NP concentrations in the polymer solutions were prepared by using toluene as solvent and having a fixed polymer concentration of 12.4 mg/mL. The weight ratio of maghemite NPs with respect to the polymer P(Sd-*b*-BMA) was varied (0, 0.1, 0.5, 1, 3, 7, and 15 wt %). The polymer was prepared at room temperature. The hybrid films were produced by spin coating on the precleaned Si substrates (parameters: acceleration time, 9 s; spin-coating time, 30 s; and spinning speed, 2000 rpm). The as-prepared hybrid films were further annealed at 160 °C for 5 h for equilibrating the morphology.[26]

2.2. Characterization Techniques. The structure of the prepared metal oxide DBC hybrid films was investigated using XRR, SEM, AFM, and TOF-GISANS. Magnetic properties were probed with a SQUID magnetometer.

2.2.1. Atomic Force Microscopy (AFM). AFM measurements were done with a JSPM-5200 AFM (Jeol) using tapping mode in ambient conditions. The applied tips had a curvature radius of less than 15 nm and were mounted onto cantilevers (ULTRASHARP NSC35/ALBS, MikroMasch) with a spring constant of 7.5 N/m and a resonance frequency of 170 kHz. All AFM data were processed and analyzed by the software WinSPM v2.14.

2.2.2. Scanning Electron Microscopy (SEM). An NVision40 FESEM by Carl Zeiss AG was used for SEM measurements with accelerating voltages of 0.4 and 4 kV at working distances of 0.9 and 1 mm. To confirm the sample homogeneity, we carried out SEM measurements on each sample in many randomly selected areas, which were located on the four corners and in the center of the square sample.

2.2.3. X-ray Reflectometry (XRR). XRR measurements were performed on a D8 ADVANCE (Bruker). The X-ray radiation was produced by a Cu anode with a wavelength of $\lambda = 0.154$ nm. The XRR curve was measured for an angular range of $0° < 2\theta < 7°$. Film thickness information was obtained by fitting the reflectivity profiles using the Parratt algorithm.[38]

2.2.4. Time-of-Flight Grazing Incidence Small Angle Neutron Scattering (TOF-GISANS). TOF-GISANS experiments were performed at the REFSANS instrument of the Helmholtz Zentrum Geesthacht at the Heinz Maier-Leibnitz Zentrum, Garching, Germany.[39−42] A fixed incident angle, under which the neutron beam impinged on the samples, was set to 0.48°, resulting in a critical wavelength for total external reflection of $\lambda_c = 0.97$ nm for the investigated P(Sd-*b*-BMA) films. Instead of a monochromatic neutron beam, a continuous neutron spectrum with a wavelength range from 0.23 to 1.22 nm was used. The wavelength discrimination of the incident beam was controlled using a high-speed double chopper system.[40] For analysis, the neutron spectra were sliced into wavelength channels with a resolution of 10% for each channel.[30] Neutrons with a short wavelength can fully penetrate our investigated films, whereas neutrons with a wavelength longer than 1.02 nm are scattered at a finite depth of less than 60 nm (the penetration depth strongly depends on the scattering length density of the investigated sample) for the selected fixed incident angle. As a consequence, depth profiles of the film structure are obtained from the TOF-GISANS data with different neutron wavelengths. The sample was placed horizontally on a sample stage. The scattering signal was recorded on a 2D ^{3}He detector. A sample−detector distance (SDD) of 10.52 m was used.[39] A beamstop was installed at a fixed position and used to block the direct beam to avoid high intensity on the detector. A schematic view of the TOF-GISANS experiment setup geometry is shown in Figure 1. Gravity effects were corrected in the data analysis procedure. To achieve sufficient statistics, the counting time for each sample was set to 24 h. All measurements were carried out at ambient conditions with no solvent involved. Structural information in different orientations is obtained from horizontal (q_y direction, parallel to the sample surface) and vertical cuts ($\alpha_i + \alpha_f$ direction, normal to the sample surface) of the 2D intensity distribution. The horizontal cuts (q_y profiles) were fitted with a model assuming a Lorentzian distribution of length scales.[12]

2.2.5. Magnetic Property Measurements (MPM). Direct current (DC) magnetization measurements as a function of temperature were performed using a superconducting quantum interference device (SQUID) magnetometer (MPMS XL-7, Quantum Design, San Diego, CA). The samples were measured while applying a range of external magnetic fields varied from −700 to 700 mT in the film plane. The measurements were carried out at temperatures of 2, 5, 20, 50, 100, and 200 K.

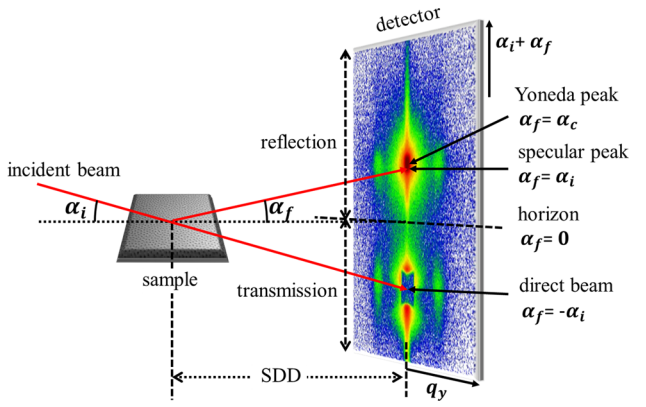

Figure 1. Schematic view of the geometry used in the TOF-GISANS experiments. The incident angle is α_i, and the exit angle is α_f. The horizon (dashed line) separates the reflected and transmitted signal.

3. RESULTS AND DISCUSSION

In the present investigation, the metal oxide−polymer hybrid films were prepared by mixing solutions with different weight ratios of PS-coated γ-Fe_2O_3 NPs and the DBC P(Sd-*b*-BMA), followed by spin coating on precleaned Si substrates. Using spin coating, the film thickness can be easily controlled by tuning parameters such as spin time, spin speed, spin speed acceleration, and solution concentration.[43,44] The film uniformity and control on the film thickness are crucial factors in application of the investigated hybrid thin film. In the present study, the spin coating parameters and the polymer concentration were chosen to create a film thickness that is almost equal to the periodic domain spacing of the employed DBC. Via several pretests, it turned out that the necessary concentration to achieve the desired film thickness was 12.4 mg/mL.

3.1. Film Thickness. Several previous investigations emphasized the effect of film thickness on the morphological orientation of DBC films.[35,45−47] Because the determination of the film thickness with a high precision is of significant interest for the investigated hybrid films, XRR data were collected. Film thickness values were extracted from the fit of these XRR data by a Parratt algorithm[38] and plotted as a function of the NP concentration in Figure 2.

The total film thickness monotonically increases from 65.9 ± 3.3 nm to 78.4 ± 2.4 nm with increasing NP concentration from 0 to 15 wt %. All preparation parameters were kept identical for the film fabrication, and the change of the viscosity of solution used for spin coating was almost not affected by the addition of the NPs. Therefore, the increase of the film thickness is mainly attributed to the extra volume due to the incorporated maghemite NPs in the metal oxide−polymer hybrid films. From the values of the Flory−Huggins interaction parameter χ (0.015) and the degree of polymerization N (2912) of the investigated DBC (χN = 43.68), the periodic domain spacing, *d*, in the bulk can be calculated with[48]

$$d \sim aN^{2/3}\chi^{1/6} \quad (1)$$

where a = 0.67 nm is the characteristic segment length, yielding a periodic domain spacing of 68 nm. Because the selected DBC is symmetric, a lamella morphology is expected. The calculated bulk periodic domain spacing of 68 nm is slightly smaller than the prepared total film thickness. According to previous investigations on thin DBC films, there are two major possibilities of the film morphology.[35,49−51] A perpendicular lamella morphology is predicted for film thicknesses $t \leq d$, which maximizes the conformational entropy of the polymer chains by allowing the equilibrium periodic domain to be expressed laterally.[35,49,50] A parallel lamella morphology is obtained for $t > d$ due to the surface boundary conditions.[35,51] Generally, the morphological orientation is mainly driven by the free energy minimization of the system.[35] As seen from Figure 2, the film thickness increases nonlinearly with the NP concentrations. At low NP concentrations (≤1 wt %), the film thickness monotonically increases at a steep slope. However, at high NP concentrations (≥7 wt %), the increase has a much lower slope. This nonlinear film thickness dependence on the NP concentration indicates that the NPs were initially incorporated into the hybrid film at low concentrations, leading to an expanded polymer chain conformation and film swelling. In contrast, at a high NP load, the added NPs mostly are not embedded within the polymer film anymore. Instead, the NPs form individually isolated random arrangements of particle aggregates on the top surface.

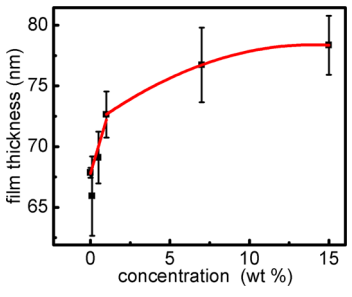

Figure 2. Thicknesses of the metal oxide−polymer hybrid films measured with XRR versus NP concentration (the solid line serves as a guide to the eye).

3.2. Surface Structures. The nanoscale surface structures of the hybrid film were examined by SEM. Because the electron penetration depth of SEM is approximately 10 nm, an SEM image shows not only the top surface morphology but also the morphology within a depth of 10 nm. Figure 3 displays selected SEM images of hybrid films with different NP concentrations. For all SEM images, dark areas and light gray areas correspond to the PSd and PBMA domains, respectively.[52]

The rarely seen, brightest surface objects are small aggregates of maghemite NPs. The morphology of the NP-free DBC film surface (Figure 3a) indicates a cylinder rather than a lamellar morphology. Several cylindrical-like structures (dark areas) are visible (Figure 3a) with an imperfect lateral ordering. In contrast, highly oriented arrays of cylindrical morphology with a long-range lateral order are observed (Figure 3b) for the hybrid film at a low NP concentration (0.5 wt %). The surface chemistry of the employed PS-coated maghemite NPs enhances the compatibility of the NPs to the PSd block, and thus, the enthalpic interaction at the interfaces between NPs and PSd domains favors mixing.[53] In general, the Flory−Huggins interaction parameter, χ, expresses the enthalpic interaction between the polymer blocks, which is generally in the range of 0.01−0.1 for most DBC systems.[54] For the investigated hybrid film system, there are three interaction parameters, $\chi_{PSd-PBMA}$, $\chi_{PSd-NPs}$ and $\chi_{PBMA-NPs}$, which represent the chemical incompatibility between PSd and PBMA, PSd and NPs, and PBMA and NPs, respectively. Due to the PS-coating on the NPs, it is assumed that the interaction parameter $\chi_{PSd-NPs}$ is approaching zero value. The interaction parameter χ for a

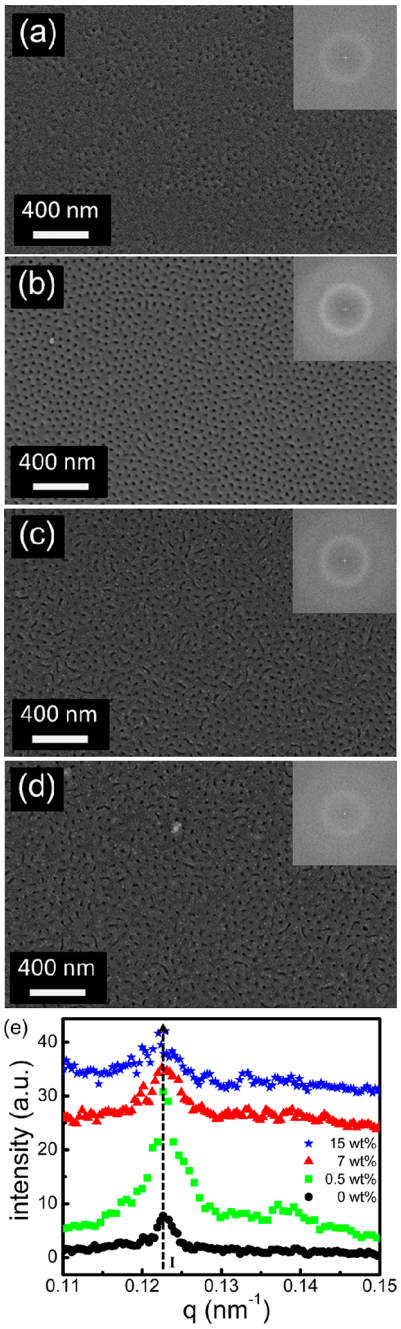

Figure 3. Selected SEM images of the hybrid films with different NP concentrations: (a) 0, (b) 0.5, (c) 7, and (d) 15 wt %. Insets are the FFT patterns of each image. (e) Power spectral density (PSD) functions obtained from radial averaging of the intensity distribution in the FFT patterns with different NP concentrations: (bottom to top) 0, 0.5, 7, and 15 wt %. The PSD profiles are shifted along the *y* axis for clarity.

mixture of PS and deuterium-substituted PS is about 1.8×10^{-4}.[55] Therefore, the PS-coated NPs are compatible with PSd. However, $\chi_{PBMA-NPs}$ is assumed to be close in value to $\chi_{PSd-PBMA}$ (0.015), assuming negligible changes in the entropic contribution. Thus, the PS-coated NPs have a high affinity for the PSd domains, about 85 times larger than for the PBMA domains.[56] Compared to the NP-free film, at rather low NP concentration (0.5 wt %), a highly ordered, densely packed cylindrical microphase separation structure is found in Figure 3b. This reveals that the structural ordering of the hybrid film is further enhanced by the incorporation of the maghemite NPs. In our previous study we observed that adding a low concentration of NPs into a polymer template is not only leading to a perfect order, but also could switch the orientation of a lamellar structure from a surface-parallel to a surface-perpendicular morphology.[57] Similarly, Lin et al. showed that the incorporation of selectively located CdSe NPs into a P(S-*b*-2VP) DBC resulted in the perpendicular orientation, because of the compensation of the surface energies difference between PS and P2VP domains.[21] In the present investigation, the highly ordered nanostructures at low NP load is attributed to the increased diffusion of the NPs within the PS domains during the annealing process, leading to an improved localization of the NP doped PS domains.

Upon further NPs upload (>0.5 wt %), the long-range ordered morphology is perturbed (Figure 3c,d) because a large number of NPs within the PS chain limit their ability to diffuse and localize. Consequently, the PS domains have less chance to optimally organize. Instead, cylinders with a deformed shape are observed. The insets in Figure 3 are the fast Fourier transform (FFT) patterns of the SEM images. The presence of ring-like FFT patterns indicates that the domains in the SEM images are isotropically distributed all over the films with a narrow distribution of the center-to-center domain spacing. At 0.5 wt % NP concentration, the ring in FFT patterns becomes better pronounced, and a second order ring appears. As the NP concentration increases, the intensity of the ring decreases, and the width increases.

In general, at low NP concentrations (0.5 wt %), the NPs are well distributed in the preferred PSd domains and swell these domains. At high NP concentrations (>0.5 wt %), the cylindrical PSd domains start to expand anisotropically, and the interfacial curvature increases. In order to accommodate more NPs, the PSd chains continue to stretch, and the initially highly ordered perpendicular cylinder morphology at low NP concentrations tends to form a parallel-like cylinder morphology at high NP concentrations. Such morphological transformations were previously reported for metal−polymer hybrid system at high NP concentrations.[58−60] At very high NP concentration (15 wt %), additional NPs cannot be accommodated within the PSd domains anymore. Thus, an ill-defined structure is observed (Figure S3, Supporting Information). In this case, the entropy penalty dominates, and the NPs are prone to form aggregates. Such behavior is in agreement with a Monte Carlo simulation, which reveals NP aggregation at high NP concentration embedded in a DBC system.[61]

Figure 3e shows a plot of the PSD functions extracted from FFT data of different NP concentrations. All PSD curves exhibit a most prominent peak intensity, *I*, at the same *q* value independent of the NP concentration. The peak *I* corresponds to the most pronounced lateral structure on the film surface, which indicates the interdomain distance of the DBC film. From the PSD curves, a lateral distance of 58 ± 2 nm is derived irrespective of the NP concentration. Thus, the incorporation of NPs does not affect the lateral domain spacing of the DBC matrix hosting the NPs. At low NP concentration (0.5 wt %), the peak *I* becomes more pronounced and narrower, which reveals highly ordered nanostructure of the related polymeric interdomains. At higher NP concentrations, the peak *I* gets less pronounced and broader but remains in the same *q* position. Thus, the presence of the NP clusters start to affect the order of

polymer nanostructure; however, it does not enlarge the domain distance.

To get the topographical information on the metal oxide–polymer hybrid films, AFM images were collected. AFM examines the surface structure with a different contrast as compared with SEM. The related surface nanomorphology of the hybrid films is shown in Figure 4 for various NP concentrations. It follows the same trend as already reported from the SEM images. For all AFM images, bright areas and dark areas correspond to the PBMA and PSd domains, respectively. At low NP concentrations, the order of the cylindrical domains increases with increasing amount of NP, whereas at high NP concentrations, order is lost by the further addition of NPs. At considerable high NP concentration (25 wt %), there are substantial NP aggregates, which form irregular sizes and disperse randomly instead of following the alignment of the PSd domains from the DBC template (Figure 4f). The NP cluster cannot be further accommodated inside the PSd cylindrical domains; therefore, the localization of the NPs is no longer correlated with the polymer template and ill-defined structures are formed. An improved visualization of the developed NP aggregates is shown in AFM images with a larger scan range (Figure S4, Supporting Information). In addition to the microphase separation structure (PSd cylindrical domains), bigger wave-like structures in micrometer scale are observed as well (Figure S4, Supporting Information).

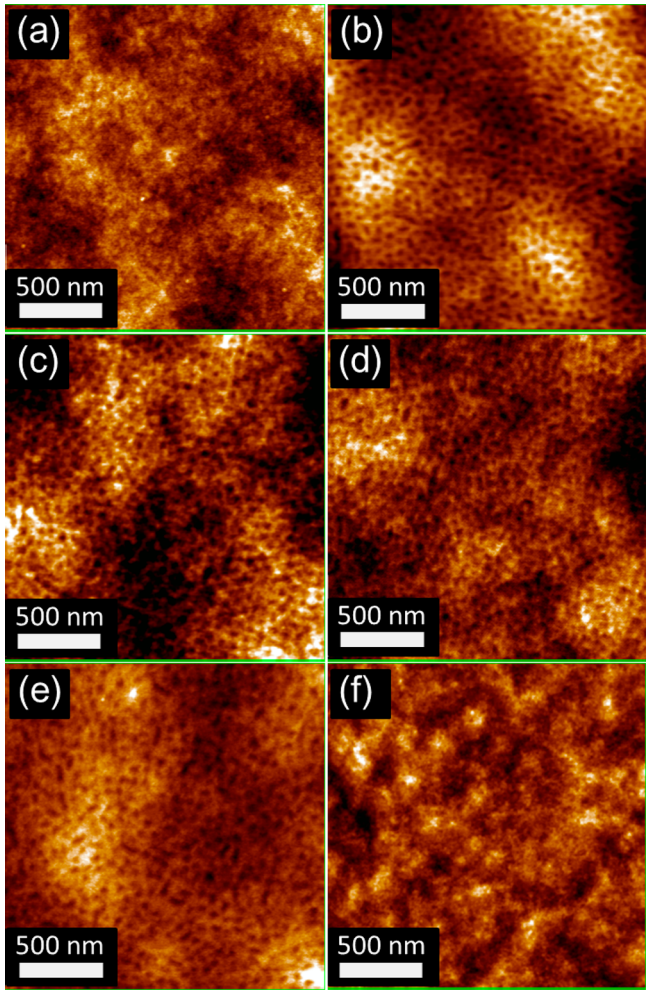

Figure 4. Selected AFM images of the hybrid films with different NP concentrations: (a) 0, (b) 0.2, (c) 0.5, (d) 3, (e) 15, and (f) 25 wt %.

In addition to visualizing the surface structure, AFM gives information about the root-mean-square (rms) surface roughness. The rms roughness of the NP-free film is 1.11 nm on the local scale probed in Figure 4a. With increasing NP concentration the rms roughness gradually increases from 1.13 to 3.48 nm. The determination of the film roughness is perturbed by the presence of large NP clusters at the surface. However, the rms roughness remains small and well below 4 nm, which indicates that all prepared films have a relatively uniform surface. AFM images with corresponding height color bar and height profile are presented in Figure S5 (Supporting Information).

3.3. Buried Structures. The formation of cylinder-like structures, the improvement of the domain alignment upon adding small amounts of NPs, and the morphological changes upon further increasing the amount of NPs has been observed on the top surface of the investigated hybrid films via real space techniques (AFM and SEM). However, these morphological features cannot be adequately explained without getting additional structural information from the polymer–substrate interface and from inside the film (buried structures). To access such structure information with AFM or SEM is very difficult. As a consequence, we applied TOF-GISANS, because TOF-GISANS not only probes the structure information from the film surface, but also gives access to the inner film morphology in terms of lateral structures and size distributions with depth-dependence.[32] Details of the TOF-GISANS technique are described elsewhere.[29] Moreover, due to the large illuminated sample volume, the information extracted with TOF-GISANS measurements has a high statistical relevance.

Figure 5 shows the 2D GISANS patterns of three DBC films with different NP concentrations (0, 0.5, and 15 wt %). Out of 18 different neutron wavelengths used to probe our samples, only five selected wavelengths are presented in Figure 5 (from top to bottom, 0.324, 0.475, 0.574, 0.774, and 1.024 nm). Generally, the lower part of the scattering images (below the dashed line) shows the transmitted intensity dominated by direct beam, which is partially shielded by a square-shaped direct beamstop for protecting the detector against the high intensity. The minimum intensity position (dashed line) represents the sample horizon. In the upper part of the scattering images (above the dashed line), the reflected GISANS signal is located.[62−64] The most intense signal in the reflected part is the specular peak, where the incident angle (α_i) and the exit angle (α_f) are equal. It shows a slight drop (within 2 pixels) in vertical position at relatively long neutron wavelengths due to the gravity effect acting on the neutron beam.[30,65] Corrections were made in the analysis to compensate for gravity. Slightly below the specular peak, a less intense Yoneda peak is observed, which is a material characteristic intensity peak. It moves along the ($\alpha_i + \alpha_f$) direction with increasing neutron wavelength.[66] The position of the Yoneda peak is strongly dependent on the material chemical composition and mass density.[67] The Yoneda peak is located at the position of the critical angle (α_c) of the investigated film and shows a wavelength, λ, dependence according to

$$\alpha_c = \lambda\left(\frac{\rho}{\pi}\right)^{1/2} \quad (2)$$

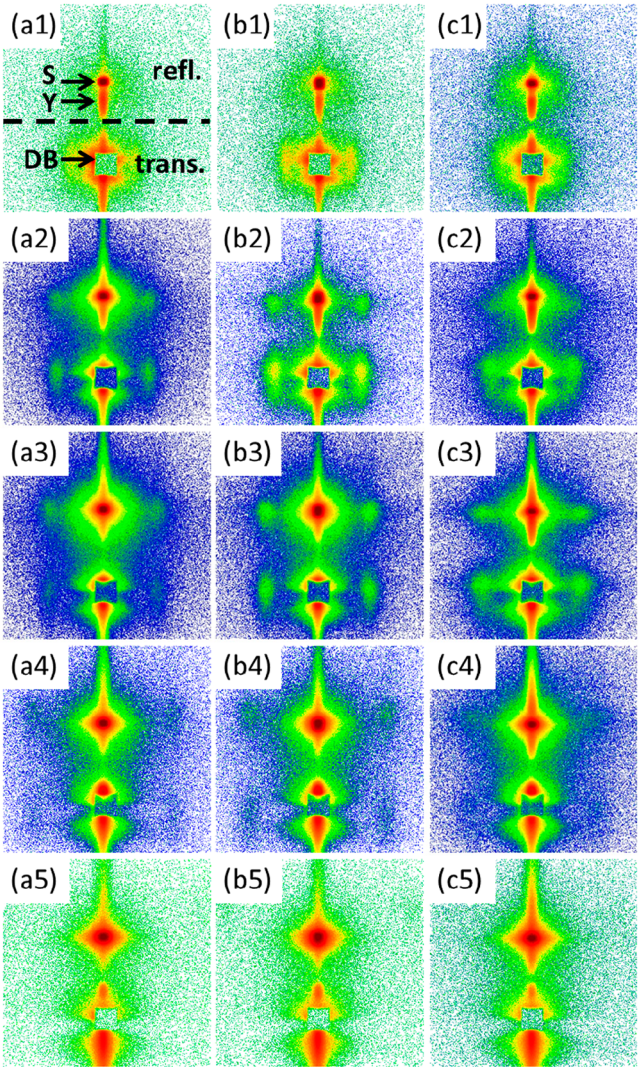

Figure 5. Selected 2D GISANS patterns of NP-free and metal oxide–polymer hybrid films with different NP concentrations: (a1–a5) 0, (b1–b5) 0.5, and (c1–c5) 15 wt %. The corresponding mean wavelengths are (top to bottom) 0.324, 0.475, 0.574, 0.774, and 1.024 nm. The position of the Yoneda peak (Y) changes at different wavelength, while the specular peak (S) has a fixed position. The direct beam (DB) is shield by a square beamstop. The transmission and reflection signals are represented above and beneath the sample horizon (dashed line), respectively.

where ρ is the neutron scattering length density of the specific materials.[29] At long wavelengths, it follows $\alpha_c \geq \alpha_i$, and thus, only a few neutrons can penetrate the film. In contrast, at shorter wavelengths (where $\alpha_c < \alpha_i$), the neutrons can systematically penetrate the samples and the measurement is bulk sensitive. From surface to bulk sensitive measurements using different wavelengths of the TOF-GISANS measurement, depth sensitive structural data are obtained. Irrespective of the neutron wavelength, along the vertical direction in the 2D GISANS data, no intensity modulation is observed, which reveals that there is no well-defined periodic structure parallel to the film surface.

Lateral structure information is extracted from two side peaks, which are observed in the 2D GISANS data. These side peaks are located at the same height along both sides of the Yoneda peak (Figure 5) and originate from the presence of a highly ordered lateral structure oriented perpendicular to the sample surface. At 0.475 nm wavelength, the intensity of the side peak, located at $q_y = 0.119$ nm^{-1}, is highly pronounced. In Figure 5, in the third row the 2D GISANS patterns change interestingly with incorporation of the NPs from left to right. At a low NP concentration (0.5 wt %, Figure 5b3), the side maxima become more intense and the overall scattered intensity is enhanced, which corresponds to a highly ordered structure of the hybrid film and an enhanced contrast of the two phases, the NPs containing PSd domains and the NP-free PBMA domains, respectively. In contrast, for higher NP concentration (15 wt %, Figure 5c3), the side peaks broaden again, indicating that the morphology is less ordered.

For further quantitative analysis, at all different wavelengths, line cuts were taken in both vertical (at $q_y = 0$) and horizontal directions (around the Yoneda peak position for the DBC of P(Sd-*b*-BMA)) for all TOF-GISANS measurements. Shown in Figure 6 is the example of the NP-free film investigated in a

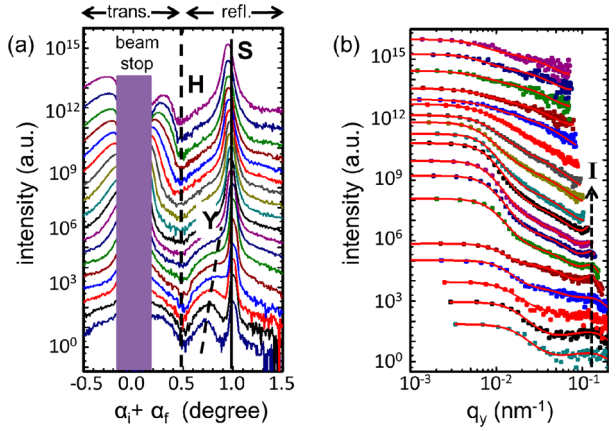

Figure 6. Line cuts from the 2D GISANS data for the NP-free film in (a) vertical direction as a function of the detector angle ($\alpha_i + \alpha_f$) and (b) horizontal direction as a function of the lateral scattering vector component q_y. The sample horizon (H), the Yoneda peak position (Y), and the specular peak position (S) are indicated by dashed lines. The horizontal line cuts are fitted (red solid lines) with a model explained in the text. The dashed line *I* guides the eye to the determined peak position. All the cuts were shifted along *y* axis for clarity. From bottom to top the neutron wavelength increases: 0.229, 0.276, 0.324, 0.375, 0.426, 0.475, 0.524, 0.574, 0.624, 0.674, 0.724, 0.774, 0.824, 0.874, 0.0924, 0.974, 1.024, and 1.074 nm.

configuration where the neutron beam impinges the film from the air side. In addition, the vertical and horizontal line cuts of all other investigated hybrid films with different NP concentrations are shown in Figure S6 (Supporting Information). Vertical cuts ($\alpha_i + \alpha_f$) offer information perpendicular to the film surface, whereas horizontal cuts (q_y) provide lateral structural information parallel to the film surface. In Figure 6a, the vertical dashed line (H) indicates the sample horizon at minimum intensity. The transmission signal and reflection signal are shown left ($\alpha_i + \alpha_f < 0.48°$) and right ($\alpha_i + \alpha_f > 0.48°$) with respect to the sample horizon, respectively. The transmitted signal originates from the transmission scattering through the neutron transparent silicon substrate. The intense direct beam is shielded by the beamstop at a scattering angle $\alpha_i + \alpha_f = 0°$. The tilted dashed line (Y) and the solid line (S) in Figure 6a represent the observed Yoneda maximum positions and the specular reflection peak positions ($2\alpha_i = 0.96$),

respectively. In Figure 6b, the horizontal line cuts provide lateral domain spacing information. All data in the horizontal cuts (points) are fitted with a model assuming prominent lateral distances with a Lorentzian distribution. The corresponding fits are represented by red solid lines in Figure 6b. Due to the different wavelengths employed in the TOF-GISANS experiments, each horizontal cut covers a different q_y range. Thus, compared to a single wavelength GISANS measurement, a large q_y range can be probed. All horizontal cuts show a smooth decay of the scattered intensity at smaller q_y values. In addition, at short wavelengths in the horizontal cuts (first four q_y profiles from bottom in Figure 6b), where α_c is far below α_i, only broad intensity peaks are observed. Broad peaks indicate an ill-defined lateral structure, which is located at the polymer−substrate interface in the present sample. As the wavelength increases, the GISANS signal becomes more sensitive to the middle part of the film. A prominent intensity peak, which is highly visible at large q_y values, shows a neat structure located in the middle part of the film. The peak position corresponds to the interdomain spacing ($D = 4\pi/\sqrt{3}q$) of 59 ± 1 nm, which originates from the microphase separation process. This value is consistent to that obtained from the FFT of the SEM images (Figure 3a). At longer wavelengths, the well-pronounced peak moves out of the accessible q_y range and is therefore no longer visible in the horizontal line cuts (Figure 6b).

Figure 7a shows the linear wavelength dependence of the critical angle for the material PSd, Si, and PBMA, which are involved in the NP-free DBC films. All the ideal expected Yoneda peak positions are obtained according to eq 2, using the ideal scattering length densities $\rho_{PSd} = 5.99 \times 10^{-4}$ nm^{-2}, $\rho_{Si} = 2.07 \times 10^{-4}$ nm^{-2}, and $\rho_{PBMA} = 5.54 \times 10^{-5}$ nm^{-2}. The experimentally observed Yoneda peak positions (Figure 7a) match the wavelength-dependent ideal expected critical angle of the PSd at short wavelengths. At longer wavelengths, no Yoneda peak position can be probed because the Yoneda peak overlaps with the high-intensity specular peak. Yoneda peak positions in agreement with the critical angle of the PSd indicate that a PSd enrichment layer at the polymer−substrate interface is present. As we discussed earlier concerning the SEM images (Figure 3), a cylindrical morphology composed of PSd domains, which are dispersed in a majority matrix of PBMA, is found at the polymer−air interface, despite the symmetric composition of the DBC with a PSd volume fraction (f_{PSd}) of 0.53. From the GISANS measurements, we conclude that a PSd enrichment layer must exist at the polymer−substrate interface. This enrichment layer induces a morphological transition to a perforated lamella.

The critical angle positions of the metal oxide−polymer hybrid films are shown in Figure S6 (Supporting Information) for some selected samples with different NP concentrations. All samples with all NP concentrations exhibit an analog behavior of the Yoneda peak position. Thus, the presence of a PSd enrichment layer at the polymer−substrate interface is not affected by embedded metal oxide NPs.

To figure out the effect of the NP concentration on the morphology inside the film, we analyzed the most pronounced intensity maximum of the horizontal line cuts. Measurements and fits for a selected neutron wavelength of 0.475 nm are shown in Figure 7b for different NP concentrations. The full set of horizontal line cuts of the 2D GISANS data from the hybrid films with different NP concentrations is shown in Figure S7 (Supporting Information). As a main feature, a well-

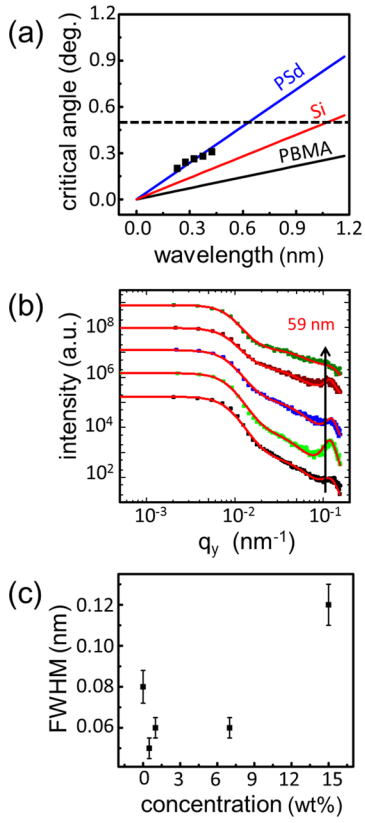

Figure 7. (a) Ideal expected critical angles positions (lines) of the surface components (PSd, Si, and PBMA) as a function of the wavelength for the NP-free DBC film. The solid squares (■) are the experimental Yoneda peak positions obtained from the vertical cuts at the corresponding wavelengths. The horizontal dashed line indicates the employed incident angle. (b) Horizontal line cuts (■) of the 2D TOF-GISANS data measured at a wavelength of 0.475 nm and corresponding fits (solid lines) of the hybrid films with NP concentrations of (bottom to top) 0, 0.5, 1, 7, and 15 wt %. (c) Full width half-maximum values obtained from the fits of the horizontal line cuts as a function of the wavelength.

pronounced peak in the intensity (I), located at large q_y values, is seen. The peak position remains unchanged. This indicates that the interdomain spacing of the polymer, which is initially created by microphase separation, is independent of the NP concentration. According to the fit results, the value of the interdomain spacing is constant at 59 ± 1 nm. However, it is obvious that the peak width (full width half-maximum, fwhm) becomes much narrower after adding a rather low concentration of NPs (0.5 wt %). Upon further NP loading, the peak width becomes broader again. At a high NP concentration (15 wt %), the peak turns to a fairly weak intensity and a very broad width. The sharpness of this peak indicates the systematic order of the nanostructure. The fwhm values are extracted from the corresponding fits of the horizontal line cuts and plotted in Figure 7c. Both the position and the width of the peak provided by the fits to the line cuts explicate the buried lateral structure of the hybrid films. In short, incorporation of selectively located NPs enhances the long-range order of the nanostructure. However, the average interdomain spacing remains constant with a systematic loss of order upon further addition of NPs. Therefore, the analysis of the TOF-GISANS data complements the observations from the real space investigation using SEM and AFM.

To clarify the morphological evolution of the metal oxide–polymer hybrid film in the nanoscale regime, we show a cross-sectional schematic representation at different NP concentrations in Figure 8. The NP-free film exhibits moderately

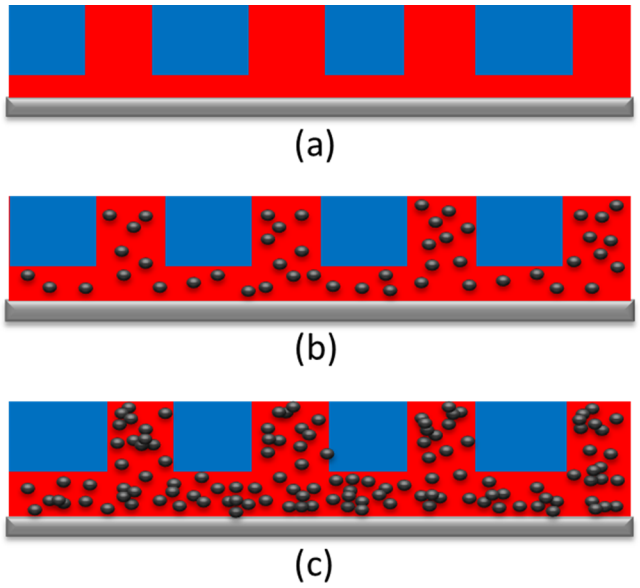

Figure 8. Schematic representation of the cross section of metal oxide–polymer hybrid films for (a) the NP-free film and (b) low and (c) high NP concentrations; (red) PSd domain, (blue) PBMA domain, (black) maghemite NPs, and (gray) silicon substrate.

ordered, perforated lamella microphase separated morphology, with a PSd enrichment layer at the polymer–substrate interface (Figure 8a). On one hand, due to a lower surface energy, PBMA and PSd prefer to segregate to the polymer–air and polymer–substrate interface, respectively.[68] On the other hand, when the polymer film thickness equals to the polymer domain spacing, the polymer is prone to form surface-perpendicular structure.[49] Weith et al. investigated the orientation of lamella in DBC films in terms of a mean-field model.[69] They found a lamella orientational transition across the block copolymer film from a parallel oriented lamella at a selective boundary to a perpendicular oriented lamella at a neutral boundary due to lower free energy.[69] At low NP concentrations (Figure 8b), the selectively embedded NPs are well distributed inside the PSd domains, which enhances the enthalpy contribution and results in highly ordered structures. Additionally, the film thickness starts to expand due to the progressive increase of the NPs deposited inside the PSd enrichment layer at the polymer–substrate interface. At high NP concentrations (Figure 8c), a highly ordered cylindrical morphology is deformed, and small clusters are formed that perturb long-range ordered structures. The film thickness increases significantly by swelling a large quantity of NPs into the PSd enrichment layer.

3.4. Magnetic Properties. SQUID magnetometry (Quantum Design MPMS) is employed to examine the magnetic properties of some selected metal oxide–polymer hybrid films. For 15 wt % NP embedded in the DBC film, the temperature dependence is probed (Figure 9). Due to the special film morphology (perforated lamella with an enrichment layer containing NP) the temperature dependence differs from the previously reported behavior, which showed saturation magnetization and slope of the magnetization curve to be independent

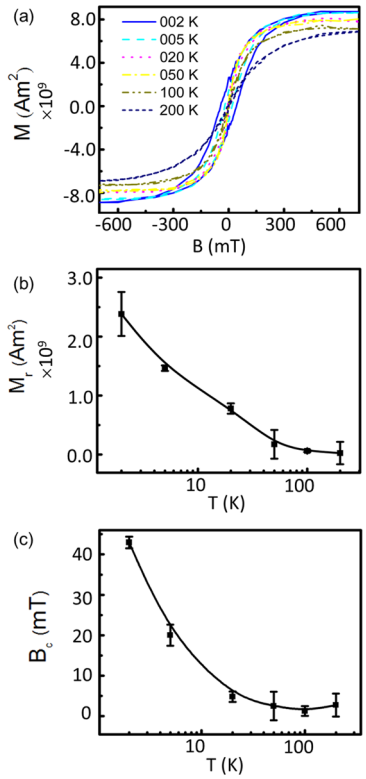

Figure 9. (a) Magnetic moments measured as a function of the external magnetic field. (b) Remanence and (c) coercivity at different temperatures for a metal oxide–polymer hybrid film with 15 wt % NP concentration (the black solid lines are guides to eyes).

from temperature in case from randomly oriented diblock copolymer matrix with γ-Fe_2O_3 NP.[28]

From Figure 9a, it is observed that the maximum magnetization (magnetic moment per unit volume) is temperature dependent and the highest value of the saturation magnetization is reached at a temperature of 2 K. The ratio of the magnetization to the saturation magnetization (M/M_s) is inversely proportional to the measured temperature. This behavior is consistent with the equation[70]

$$\frac{M}{M_s} = \frac{\mu B}{3k_B T} \tag{3}$$

where M is the magnetization, M_s is the saturation magnetization, μ is the magnetic moment, B is the magnetic field, k_B is the Boltzmann constant, and T is the temperature. The remanence (Figure 9b), which is extracted from the measured hysteresis loops (Figure 9a), is temperature dependent as well. The remanence reduces strongly with increasing temperature, whereas a weaker decrease was reported for other diblock copolymer films with embedded iron oxide nanoparticles.[28] Owing to thermal agitation, the coercive fields (Figure 9c) decrease strongly with increasing temperature. Below a certain characteristic temperature, the hysteresis in the magnetization data is seen, which is characteristic for a superparamagnetic behavior.[71] Néel defined the specific characteristic temperature as a blocking temperature of superparamagnetic particles, which is delineated by the Néel–Brown expression[72]

$$\tau = \tau_0 \exp\left(\frac{KV}{k_B T}\right)$$

dx.doi.org/10.1021/am505143h | ACS Appl. Mater. Interfaces 2014, 6, 18152–18162

where τ is a relaxation time, τ_0 is the inverse attempt frequency, K is the uniaxial anisotropy, and V is the particle volume.

Magnetic moments measured at 2 K for selected samples with different NP concentrations are shown in Figure 10a. The

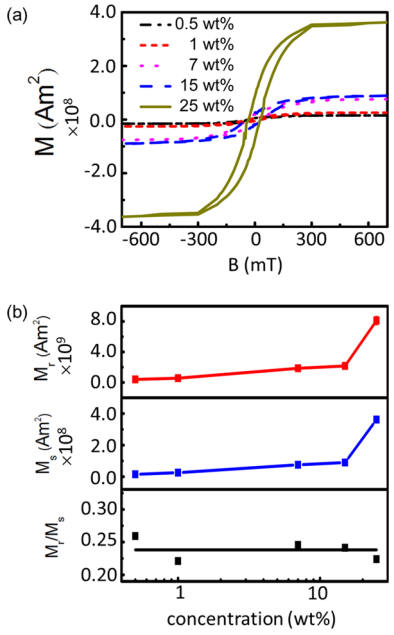

Figure 10. (a) Magnetic moments measured as a function of external magnetic field at 2 K for different NP concentrations: 0.5, 1, 7, 15, and 25 wt %. (b) The remanence, M_r, saturation magnetization, M_s, and relative remanence, M_r/M_s, extracted from magnetic moments as a function of NP concentration at 2 K.

NP concentration dependence of the remanence, M_r, saturation magnetization, M_s, which are extracted from Figure 10a, and calculated relative remanence, M_r/M_s are shown in Figure 10b. Within experimental error, M_r and M_s show the same trend of being monotonically increasing with NP concentration. However, the relative remanence (M_r/M_s) remains constant irrespective of concentration. Such behavior was reported for diblock copolymer films with embedded iron oxide NP.[73] Thus, taking all above results of magnetic properties into consideration, the hybrid film system follows a superparamagnetic behavior.[74] The related superparamagnetic behavior can be explicated in details with a modified Stoner–Wohlfarth–Néel model.[29,72,73] In contrast to a randomly oriented diblock copolymer film matrix, for the perforated lamella with an enrichment layer containing NPs, the developed thermodynamics of the superspins was not modified by either an elastic torsion mechanism or a statistical distribution of the anisotropy constants, which was observed in our previous investigations.[29,72,73]

4. CONCLUSIONS

Superparamagnetic metal oxide–polymer hybrid films of PS-coated maghemite NPs embedded in the P(Sd-*b*-BMA) DBC template are systematically investigated using XRR, SEM, AFM, TOF-GISANS, and SQUID in the case of the special morphology of a perforated lamella with an enrichment layer containing NPs. Using a film thickness comparable to that of the periodic interdomain spacing of the investigated DBC, this special film morphology has been obtained. At low NP concentrations, a highly ordered arrangement of maghemite NPs in the polymer films is obtained via a self-assembly process, and the PS-coated NPs are selectively incorporated into the PSd domains of the DBC, while the interdomain distance remains almost constant, irrespective of NP concentration. Keeping lateral nanostructures at the DBC film surface constant, irrespective of the NP load is interesting for applications as it does not change the periodicity of the magnetic nanostructure.

Furthermore, because of the modification of the system enthalpy, the ordered and perpendicular orientation of nanostructure was enhanced with the presence of a low amount of NPs. At high NP concentrations, iron oxide NP clusters were formed, which perturbed the initially developed long-range ordered structure. Interestingly, a large quantity of NPs was deposited into the PSd enrichment layer at the polymer–substrate interface, which resulted in an overall pronounced film thickness increase. The main advantage of the current process is the simplicity and high reproducibility of the film preparation. The magnetic properties of the hybrid films show superparamagnetic behavior, which renders the present investigated hybrid film system interesting for a number of applications in fields as diverse as medical devices, magnetic sensors, and magnetic memory devices.

■ ASSOCIATED CONTENT

Supporting Information

Additional experimental results including SAXS, Mössbauer spectra of maghemite (γ-Fe_2O_3)NPs; SEM and AFM images of the metal oxide–polymer hybrid films; and Yoneda peak positions and horizontal line cuts extracted from the TOF-GISANS data of the hybrid films with different NP concentrations. This material is available free of charge via the Internet at http://pubs.acs.org.

■ AUTHOR INFORMATION

Corresponding Author

*E-mail: muellerb@ph.tum.de. Phone: +49 89 289 12451. Fax: +49 89 289 12 473.

Notes

The authors declare no competing financial interest.

■ ACKNOWLEDGMENTS

This work was supported by the German Ministry of Research and Education (BMBF, Grant 03DU03MU). Y.Y. and B.S. acknowledge the China Scholarship Council (CSC). We thank Prof. Friedrich E. Wagner for his help with the Mössbauer measurements. We thank Professor Alexander Holleitner and Peter Weiser for the chance to carry out SEM measurements.

■ REFERENCES

(1) Park, S.; Lee, D. H.; Xu, J.; Kim, B.; Hong, S. W.; Jeong, U.; Xu, T.; Russell, T. P. Macroscopic 10-Terabit-per-Square-Inch Arrays from Block Copolymers with Lateral Order. *Science* **2009**, *323*, 1030–1033.

(2) Jang, Y. H.; Xin, X.; Byun, M.; Jang, Y. J.; Lin, Z.; Kim, D. H. An Unconventional Route to High-Efficiency Dye-Sensitized Solar Cells via Embedding Graphitic Thin Films into TiO_2 Nanoparticle Photoanode. *Nano Lett.* **2011**, *12*, 479–485.

(3) Zhang, Z.; Yang, J.-L.; Friedrich, K. Creep Resistant Polymeric Nanocomposites. *Polymer* **2004**, *45*, 3481–3485.

(4) Hussain, F.; Hojjati, M.; Okamoto, M.; Gorga, R. E. Review Article: Polymer-Matrix Nanocomposites, Processing, Manufacturing, and Application: An Overview. *J. Compos. Mater.* **2006**, *40*, 1511–1575.

(5) Avalle, M.; Belingardi, G.; Montanini, R. Characterization of Polymeric Structural Foams under Compressive Impact Loading by Means of Energy-Absorption Diagram. *Int. J. Impact Eng.* **2001**, *25*, 455−472.
(6) Wei, Q.; Lin, Y.; Anderson, E. R.; Briseno, A. L.; Gido, S. P.; Watkins, J. J. Additive-Driven Assembly of Block Copolymer−Nanoparticle Hybrid Materials for Solution Processable Floating Gate Memory. *ACS Nano* **2012**, *6*, 1188−1194.
(7) Kortaberria, G.; Arruti, P.; Jimeno, A.; Mondragon, I.; Sangermano, M. Local Dynamics in Epoxy Coatings Containing Iron Oxide Nanoparticles by Dielectric Relaxation Spectroscopy. *J. Appl. Polym. Sci.* **2008**, *109*, 3224−3229.
(8) Kortaberria, G.; Arruti, P.; Mondragon, I.; Vescovo, L.; Sangermano, M. Dynamics of in Situ Synthetized Silver-Epoxy Nanocomposites as Studied by Dielectric Relaxation Spectroscopy. *J. Appl. Polym. Sci.* **2011**, *120*, 2361−2367.
(9) Vescovo, L.; Sangermano, M.; Scarazzini, R.; Kortaberria, G.; Mondragon, I. In-Situ-Synthetized Silver/Epoxy Nanocomposites: Electrical Characterization by Means of Dielectric Spectroscopy. *Macromol. Chem. Phys.* **2010**, *211*, 1933−1939.
(10) Kätelhön, E.; Compton, R. G. Nanoparticles in Sensing Applications: On What Timescale Do Analyte Species Adsorb on the Particle Surface? *Analyst* **2014**, *139*, 2411−2415.
(11) Lu, A. H.; Salabas, E. L.; Schüth, F. Magnetic Nanoparticles: Synthesis, Protection, Functionalization, and Application. *Angew. Chem., Int. Ed.* **2007**, *46*, 1222−1244.
(12) Yao, Y.; Metwalli, E.; Niedermeier, M. A.; Opel, M.; Lin, C.; Ning, J.; Perlich, J.; Roth, S. V.; Müller-Buschbaum, P. Nano- and Microstructures of Magnetic Field-Guided Maghemite Nanoparticles in Diblock Copolymer Films. *ACS Appl. Mater. Interfaces* **2014**, *6*, 5244−5254.
(13) Ganesan, V.; Jayaraman, A. Theory and Simulation Studies of Effective Interactions, Phase Behavior, and Morphology in Polymer Nanocomposites. *Soft Matter* **2014**, *10*, 13−38.
(14) Ross, C. A.; Berggren, K. K.; Cheng, J. Y.; Jung, Y. S.; Chang, J.-B. Three-Dimensional Nanofabrication by Block Copolymer Self-Assembly. *Adv. Mater.* **2014**, *26*, 4386−4396.
(15) Horechyy, A.; Zafeiropoulos, N. E.; Nandan, B.; Formanek, P.; Simon, F.; Kiriy, A.; Stamm, M. Highly Ordered Arrays of Magnetic Nanoparticles Prepared via Block Copolymer Assembly. *J. Mater. Chem.* **2010**, *20*, 7734−7741.
(16) Balazs, A. C.; Emrick, T.; Russell, T. P. Nanoparticle Polymer Composites: Where Two Small Worlds Meet. *Science* **2006**, *314*, 1107−1110.
(17) Etxeberria, H.; Fernandez, R.; Zalakain, I.; Mondragon, I.; Eceiza, A.; Kortaberria, G. Effect of CdSe Nanoparticle Addition on Nanostructuring of PS-*b*-P4VP Copolymer via Solvent Vapor Exposure. *J. Colloid Interface Sci.* **2014**, *416*, 25−29.
(18) Etxeberria, H.; Zalakain, I.; Mondragon, I.; Eceiza, A.; Kortaberria, G. Generation of Nanocomposites Based on Polystyrene-Grafted CdSe Nanoparticles by Grafting through and Block Copolymer. *Colloid Polym. Sci.* **2013**, *291*, 1881−1886.
(19) Lee, J. Y.; Thompson, R. B.; Jasnow, D.; Balazs, A. C. Effect of Nanoscopic Particles on the Mesophase Structure of Diblock Copolymers. *Macromolecules* **2002**, *35*, 4855−4858.
(20) Fan, H.; Jin, Z. Selective Swelling of Block Copolymer Nanoparticles: Size, Nanostructure, and Composition. *Macromolecules* **2014**, *47*, 2674−2681.
(21) Lin, Y.; Böker, A.; He, J.; Sill, K.; Xiang, H.; Abetz, C.; Li, X.; Wang, J.; Emrick, T.; Long, S.; Wang, Q.; Balazs, A.; Russell, T. P. Self-Directed Self-Assembly of Nanoparticle/Copolymer Mixtures. *Nature* **2005**, *434*, 55−59.
(22) Lo, C.-T.; Lin, W.-T. Effect of Rod Length on the Morphology of Block Copolymer/Magnetic Nanorod Composites. *J. Phys. Chem. B* **2013**, *117*, 5261−5270.
(23) Aissou, K.; Alnasser, T.; Pecastaings, G.; Goglio, G.; Toulemonde, O.; Mornet, S.; Fleury, G.; Hadziioannou, G. Hierarchical Assembly of Magnetic $L1_0$-ordered FePt Nanoparticles in Block Copolymer Thin Films. *J. Mater. Chem. C* **2013**, *1*, 1317−1321.
(24) Akcora, P.; Zhang, X.; Varughese, B.; Briber, R. M.; Kofinas, P. Structural and Magnetic Characterization of Norbornene−Deuterated Norbornene Dicarboxylic Acid Diblock Copolymers Doped with Iron Oxide Nanoparticles. *Polymer* **2005**, *46*, 5194−5201.
(25) Abul Kashem, M. M.; Perlich, J.; Schulz, L.; Roth, S.; Petry, W.; Müller-Buschbaum, P. Maghemite Nanoparticles on Supported Diblock Copolymer Nanostructures. *Macromolecules* **2007**, *40*, 5075−5083.
(26) Abul Kashem, M. M.; Perlich, J.; Diethert, A.; Wang, W.; Memesa, M.; Gutmann, J. S.; Majkova, E.; Capek, I. c.; Roth, S. V.; Petry, W.; Müller-Buschbaum, P. Array of Magnetic Nanoparticles via Particle Co-operated Self-Assembly in Block Copolymer Thin Film. *Macromolecules* **2009**, *42*, 6202−6208.
(27) Abul Kashem, M. M.; Perlich, J.; Schulz, L.; Roth, S.; Müller-Buschbaum, P. Correlated Roughness in Polymer Films Containing Maghemite Nanoparticles. *Macromolecules* **2008**, *41*, 2186−2194.
(28) Xia, X.; Metwalli, E.; Ruderer, M. A.; Körstgens, V.; Busch, P.; Böni, P.; Müller-Buschbaum, P. Nanostructured Diblock Copolymer Films with Embedded Magnetic Nanoparticles. *J. Phys.: Condens. Matter* **2011**, *23*, 254203.
(29) Müller-Buschbaum, P.; Metwalli, E.; Moulin, J.-F.; Kudryashov, V.; Haese-Seiller, M.; Kampmann, R. Time of Flight Grazing Incidence Small Angle Neutron Scattering. *Eur. Phys. J.: Spec. Top.* **2009**, *167*, 107−112.
(30) Kaune, G.; Haese-Seiller, M.; Kampmann, R.; Moulin, J.-F.; Zhong, Q.; Müller-Buschbaum, P. TOF-GISANS Investigation of Polymer Infiltration in Mesoporous TiO_2 Films for Photovoltaic Applications. *J. Polym. Sci., Part B: Polym. Phys.* **2010**, *48*, 1628−1635.
(31) Kreuzpaintner, W.; Moulin, J.-F.; Lott, D.; Kampmann, R.; Haese-Seiller, M.; Störmer, M.; Schreyer, A. Time-of-Flight Grazing Incidence Small Angle Neutron Scattering on Gd Nanowires. *Eur. Phys. J.: Spec. Top.* **2009**, *167*, 73−79.
(32) Müller-Buschbaum, P.; Kaune, G.; Haese-Seiller, M.; Moulin, J.-F. Morphology Determination of Defect-Rich Diblock Copolymer Films with Time-of-Flight Grazing-Incidence Small-Angle Neutron Scattering. *J. Appl. Crystallogr.* **2014**, *47*, 1228−1237.
(33) Metwalli, E.; Moulin, J.-F.; Rauscher, M.; Kaune, G.; Ruderer, M. A.; Van Burck, U.; Haese-Seiller, M.; Kampmann, R.; Müller-Buschbaum, P. Structural Investigation of Thin Diblock Copolymer Films Using Time-of-Flight Grazing-Incidence Small-Angle Neutron Scattering. *J. Appl. Crystallogr.* **2010**, *44*, 84−92.
(34) Hamley, I. W., Ed. *Developments in Block Copolymer Science and Technology*, 1st ed; John Wiley & Sons, Ltd.: West Sussex, 2004.
(35) Fasolka, M. J.; Banerjee, P.; Mayes, A. M.; Pickett, G.; Balazs, A. C. Morphology of Ultrathin Supported Diblock Copolymer Films: Theory and Experiment. *Macromolecules* **2000**, *33*, 5702−5712.
(36) Cabuil, V.; Hochart, N.; Perzynski, R.; Lutz, P. J. In *Trends in Colloid and Interface Science VIII*; Ottewill, R. H.; Rennie, A. R., Eds.; Springer-Verlag: New York, 1994; Chapter 15, pp 71−74.
(37) Metwalli, E.; Moulin, J.-F.; Perlich, J.; Wang, W.; Diethert, A.; Roth, S.; Müller-Buschbaum, P. Polymer-Template-Assisted Growth of Gold Nanowires Using a Novel Flow-Stream Technique. *Langmuir* **2009**, *25*, 11815−11821.
(38) Parratt, L. G. Surface Studies of Solids by Total Reflection of X-Rays. *Phys. Rev.* **1954**, *95*, 359−369.
(39) Kampmann, R.; Haese-Seiller, M.; Kudryashov, V.; Deriglazov, V.; Tristl, M.; Daniel, C.; Toperverg, B.; Schreyer, A.; Sackmann, E. The Potential of the Horizontal Reflectometer REFSANS/FRM-II for Measuring Low Reflectivity and Diffuse Surface Scattering. *Phys. B* **2004**, *350*, E763−E766.
(40) Kampmann, R.; Haese-Seiller, M.; Kudryashov, V.; Nickel, B.; Daniel, C.; Fenzl, W.; Schreyer, A.; Sackmann, E.; Raedler, J. Horizontal TOF-Neutron Reflectometer REFSANS at FRM-II Munich/Germany: First Tests and Status. *Phys. B* **2006**, *385*, 1161−1163.
(41) Kampmann, R.; Haese-Seiller, M.; Kudryashov, V.; Deriglazov, V.; Syromiatnikov, V.; Tristl, M.; Toperverg, B.; Okorokov, A.;

Schreyer, A.; Sackmann, E. Perspectives for Polarised Reflectometry at the Novel Reflectometer REFSANS at FRM-II in Munich/Germany. *Phys. B* **2003**, *335*, 274−277.
(42) Kampmann, R.; Haese-Seiller, M.; Marmotti, M.; Burmester, J.; Deriglazov, V.; Syromiatnikov, V.; Okorokov, A.; Frisius, F.; Tristl, M.; Sackmann, E. The Novel Reflectometer REFSANS for Analyses of Liquid and Soft Surfaces at the New Research Reactor FRM-II in Munich, Germany. *Appl. Phys. A: Mater. Sci. Process.* **2002**, *74*, s249−s251.
(43) Flack, W. W.; Soong, D. S.; Bell, A. T.; Hess, D. W. A Mathematical Model for Spin Coating of Polymer Resists. *J. Appl. Phys.* **1984**, *56*, 1199−1206.
(44) Sahu, N.; Parija, B.; Panigrahi, S. Fundamental Understanding and Modeling of Spin Coating Process: A Review. *Indian J. Phys.* **2009**, *83*, 493−502.
(45) Kim, H.-C.; Hinsberg, W. D. Surface Patterns from Block Copolymer Self-Assembly. *J. Vac. Sci. Technol., A* **2008**, *26*, 1369−1382.
(46) Vignaud, G.; Gibaud, A.; Grübel, G.; Joly, S.; Ausserre, D.; Legrand, J.; Gallot, Y. Ordering of Diblock PS-PBMA Thin Films: An X-Ray Reflectivity Study. *Phys. B* **1998**, *248*, 250−257.
(47) Ramos, J. A.; Espósito, L. H.; Fernández, R.; Zalakain, I.; Goyanes, S.; Avgeropoulos, A.; Zafeiropoulos, N. E.; Kortaberria, G.; Mondragon, I. Block Copolymer Concentration Gradient and Solvent Effects on Nanostructuring of Thin Epoxy Coatings Modified with Epoxidized Styrene−Butadiene−Styrene Block Copolymers. *Macromolecules* **2012**, *45*, 1483−1491.
(48) Semenov, A. N. Contribution to the Theory of Microphase Layering in Block-Copolymer Melts. *J. Exp. Theor. Phys.* **1985**, *61*, 733−742.
(49) Kim, S. O.; Solak, H. H.; Stoykovich, M. P.; Ferrier, N. J.; de Pablo, J. J.; Nealey, P. F. Epitaxial Self-Assembly of Block Copolymers on Lithographically Defined Nanopatterned Substrates. *Nature* **2003**, *424*, 411−414.
(50) Kellogg, G. J.; Walton, D. G.; Mayes, A. M.; Lambooy, P.; Russell, T. P.; Gallagher, P. D.; Satija, S. K. Observed Surface Energy Effects in Confined Diblock Copolymers. *Phys. Rev. Lett.* **1996**, *76*, 2503−2506.
(51) Coulon, G.; Russell, T. P.; Deline, V. R.; Green, P. F. Surface-Induced Orientation of Symmetric, Diblock Copolymers: A Secondary Ion Mass-Spectrometry Study. *Macromolecules* **1989**, *22*, 2581−2589.
(52) Lopes, W. A.; Jaeger, H. M. Hierarchical Self-Assembly of Metal Nanostructures on Diblock Copolymer Scaffolds. *Nature* **2001**, *414*, 735−738.
(53) Reddy, B. *Advances in Diverse Industrial Applications of Nanocomposites*, 1st ed; InTech: Rijeka, 2011.
(54) Jones, R. A. L. *Soft Condensed Matter*, 1st ed; Oxford University Press: New York, 2002.
(55) Mark, J.; Ngai, K.; Graessley, W.; Mandelkern, L.; Samulski, E.; Koenig, J.; Wignall, G. *Physical Properties of Polymers*, 3rd ed; Cambridge University Press: Cambridge, 2004.
(56) Chiu, J. J.; Kim, B. J.; Kramer, E. J.; Pine, D. J. Control of Nanoparticle Location in Block Copolymers. *J. Am. Chem. Soc.* **2005**, *127*, 5036−5037.
(57) Lauter-Pasyuk, V.; Lauter, H.; Gordeev, G.; Müller-Buschbaum, P.; Toperverg, B.; Petry, W.; Jernenkov, M.; Petrenko, A.; Aksenov, V. Parallel and Perpendicular Lamellar Phases in Copolymer−Nanoparticle Multilayer Structures. *Phys. B* **2004**, *350*, E939−E942.
(58) Yeh, S.-W.; Wei, K.-H.; Sun, Y.-S.; Jeng, U.-S.; Liang, K. S. CdS Nanoparticles Induce a Morphological Transformation of Poly(styrene-*b*-4-vinylpyridine) from Hexagonally Packed Cylinders to a Lamellar Structure. *Macromolecules* **2005**, *38*, 6559−6565.
(59) Ho, R.-M.; Lin, T.; Jhong, M.-R.; Chung, T.-M.; Ko, B.-T.; Chen, Y.-C. Phase Transformation in Self-Assembly of the Gold/Poly(4-vinylpyridine)-*b*-poly(ε-caprolactone) Hybrid System. *Macromolecules* **2005**, *38*, 8607−8610.
(60) Kim, B. J.; Chiu, J. J.; Yi, G. R.; Pine, D. J.; Kramer, E. J. Nanoparticle-Induced Phase Transitions in Diblock-Copolymer Films. *Adv. Mater.* **2005**, *17*, 2618−2622.
(61) Huh, J.; Ginzburg, V. V.; Balazs, A. C. Thermodynamic Behavior of Particle/Diblock Copolymer Mixtures: Simulation and Theory. *Macromolecules* **2000**, *33*, 8085−8096.
(62) Müller-Buschbaum, P. Grazing Incidence Small-Angle Neutron Scattering: Challenges and Possibilities. *Polym. J.* **2013**, *45*, 34−42.
(63) Müller-Buschbaum, P.; Maurer, E.; Bauer, E.; Cubitt, R. Surface versus Confinement Induced Morphology Transition in Triblock Copolymer Films: A Grazing Incidence Small Angle Neutron Scattering Investigation. *Langmuir* **2006**, *22*, 9295−9303.
(64) Müller-Buschbaum, P.; Schulz, L.; Metwalli, E.; Moulin, J.-F.; Cubitt, R. Lateral Structures of Buried Interfaces in ABA-Type Triblock Copolymer Films. *Langmuir* **2008**, *24*, 7639−7644.
(65) Rawolle, M.; Sarkar, K.; Niedermeier, M. A.; Schindler, M.; Lellig, P.; Gutmann, J. S.; Moulin, J.-F.; Haese-Seiller, M.; Wochnik, A. S.; Scheu, C.; Müller-Buschbaum, P. Infiltration of Polymer Hole-Conductor into Mesoporous Titania Structures for Solid-State Dye-Sensitized Solar Cells. *ACS Appl. Mater. Interfaces* **2013**, *5*, 719−729.
(66) Yoneda, Y. Anomalous Surface Reflection of X-rays. *Phys. Rev.* **1963**, *131*, 2010−2013.
(67) Niedermeier, M.; Magerl, D.; Zhong, Q.; Nathan, A.; Körstgens, V.; Perlich, J.; Roth, S.; Müller-Buschbaum, P. Combining Mixed Titania Morphologies into a Complex Assembly Thin Film by Iterative Block-Copolymer-Based Sol−Gel Templating. *Nanotechnology* **2012**, *23*, 145602.
(68) Lauter-Pasyuk, V.; Lauter, H.; Ausserre, D.; Gallot, Y.; Cabuil, V.; Kornilov, E.; Hamdoun, B. Effect of Nanoparticle Size on the Internal Structure of Copolymer-Nanoparticles Composite Thin Films Studied by Neutron Reflection. *Phys. B* **1998**, *241−243*, 1092−1094.
(69) Weith, V.; Krekhov, A.; Zimmermann, W. Stability and Orientation of Lamellae in Diblock Copolymer Films. *J. Chem. Phys.* **2013**, *139*, 054908.
(70) Blundell, S. *Magnetism in Condensed Matter*, 1st ed; Oxford University Press: New York, 2001.
(71) Bedanta, S.; Kleemann, W. Supermagnetism. *J. Phys. D: Appl. Phys.* **2009**, *42*, 013001.
(72) Néel, L. Théorie du Traînage Magnétique des Ferromagnétiques en Grains Fins avec Applications aux Terres Cuites. *Ann. Géophys* **1949**, *5*, 99−136.
(73) Schulz, L.; Schirmacher, W.; Omran, A.; Shah, V.; Böni, P.; Petry, W.; Müller-Buschbaum, P. Elastic Torsion Effects in Magnetic Nanoparticle Diblock−Copolymer Structures. *J. Phys.: Condens. Matter* **2010**, *22*, 346008.
(74) Bean, C. P.; Jacobs, I. S. Magnetic Granulometry and Super-Paramagnetism. *J. Appl. Phys.* **1956**, *27*, 1448−1452.